Journal of Applied Physics

RESEARCH ARTICLE | FEBRUARY 28 2025

Structure–property relations of binary ferrite melts

Special Collection: Disordered Materials at the Atomic Scale

C. J. Benmore ✉ ; C. Shi; O. L. G. Alderman ; J. P. Harvey; D. Lipke ; J. K. R. Weber

J. Appl. Phys. 137, 085903 (2025)
https://doi.org/10.1063/5.0242452
CHORUS

Journal of Applied Physics ARTICLE pubs.aip.org/aip/jap

Structure–property relations of binary ferrite melts

Cite as: J. Appl. Phys. **137**, 085903 (2025); doi: 10.1063/5.0242452
Submitted: 4 October 2024 · Accepted: 5 February 2025 ·
Published Online: 28 February 2025

C. J. Benmore,[1,2,a)] C. Shi,[2,3] O. L. G. Alderman,[4] J. P. Harvey,[5] D. Lipke,[6] and J. K. R. Weber[2,7]

AFFILIATIONS

[1]C-STEEL Center for Steel Electrification by Electrosynthesis, Argonne National Laboratory, Lemont Illinois 60439, USA
[2]X-Ray Science Division, Advanced Photon Source, Argonne National Laboratory, Lemont Illinois 60439, USA
[3]Beijing Synchrotron Radiation Facility, Institute of High Energy Physics, Chinese Academy of Sciences, Beijing 100049, People's Republic of China
[4]ISIS Neutron and Muon Source, Rutherford Appleton Laboratory, Chilton, Didcot, Oxon OX11 0QX, United Kingdom
[5]Centre for Research in Computational Thermochemistry, Department of Chemical Engineering, Polytechnique Montréal, Succursale, Montréal, Québec C.P. 6079, Canada
[6]Department of Materials Science and Engineering, Missouri University of Science and Technology, Rolla, Missouri 65409, USA
[7]Materials Development, Inc., Arlington Heights, Illinois 60202, USA

Note: This paper is part of the special topic on Disordered Materials at the Atomic Scale.
[a)]**Author to whom correspondence should be addressed:** benmore@anl.gov

ABSTRACT

Molten ferrite systems are used in the smelting and refining processes in steelmaking, to reduce the loss of metals in slags and to accelerate reaction rates. Here, high-energy x-ray diffraction experiments have been performed on aerodynamically levitated molten spheres of $43BaO–57FeO_X$ and $43SrO–57FeO_X$ at 1873 K using laser beam heating. The composition was varied within the range of x = 1–1.5 by changing the oxygen partial pressure of the levitation gas. The corresponding x-ray pair distribution functions have been interpreted using empirical potential structure refinement (EPSR) modeling. In oxygen-rich melts (x = 1.5), our EPSR models indicate very similar structures for the different alkaline-earth liquids, with both the Ba–O and Sr–O coordination numbers to be ∼8.4 and the total Fe–O coordination numbers ∼5.7. However, our models show that in reducing environments, the Fe^{3+} and Fe^{2+} ions exhibit very different behaviors in the Ba- and Sr-ferrite liquids. In the Ba-ferrite melt, the Fe^{3+}–O coordination number decreases from 5.7 (at x = 1.5) to 5.2 (at x = 1.07), whereas Fe^{2+}–O remains constant at ∼5.0 across the same compositional range. In the Sr melts, both the Fe^{2+}–O and Fe^{3+}–O coordination numbers rise from ∼5.7 (at x = 1.5) to 6.3 (at x = 1.07). All models show the structures to be heterogeneous with intertwined nanometer sized clusters or channels of Ba/Sr–O and Fe–O polyhedra that grow as oxygen content is reduced. Changes in the viscosity and electrical properties are interpreted in terms of the number of bridging and non-bridging oxygens associated with FeO_4 tetrahedra and concentration of charge carriers, respectively.

I. INTRODUCTION

Molten alkaline-earth ferrites are used in smelting iron ores as part of the steelmaking process, to minimize the loss of iron in slag, reduce the amount of slag produced, and increase reaction rates compared to non-fluxed silica-rich slags.[1] These reduction reactions are limited by the liquid and gas mass transfers,[2] which are, in turn, highly correlated to the kinematic viscosity of the slag. For example, adding calcium oxide to liquid iron oxides increases the reduction rate of iron using CO gas by an order of magnitude.[2] This chemical reaction relates to the final step of the smelting process, in which the high temperature melt is exposed to a reducing gas environment to remove oxygen atoms from the liquid metal. The main motivation of this paper is to search for connections between the physical properties of these binary ferrite liquids, e.g., density, viscosity, and conductivity, and the local atomic bonding, in particular the Fe–O coordination number. A clearer understanding of structure–property relations during the iron-making process could provide insights into cheaper, decarbonized manufacturing routes that occur at lower temperatures. However, liquid ferrite structures can be complex because iron is known to occur in both ferric (Fe^{3+}) and ferrous (Fe^{2+})

oxidation states, and both have been shown to exist in multiple coordination environments with oxygen, including fivefold coordination in the corresponding crystalline BaO- and SrO-ferrites.[3–6] However, previous studies have used incorrect assumptions on the distribution of either four or six coordinate oxygen by Fe^{3+}, based on iron silicate crystal structures,[7,8] which requires revision. The situation is compounded because iron redox and coordination environments are known to depend on temperature, composition, and oxygen partial pressure.[9–11]

Probing the Fe–O coordination in the liquid state at temperatures ≥1600 K is experimentally challenging, but necessary, because these compositions do not easily form glasses.[11] This paper builds on our previous work using laser-heating combined with aerodynamic levitation and high-energy x-ray diffraction to perform *in situ* studies of the structure of liquids.[9,12] Our methodology enables the study of reactive materials at high temperatures and under controlled oxygen partial pressures, where no suitable containers exist. Shi *et al.* used empirical potential structure refinement (EPSR) to extract average Fe–O coordination numbers from high-energy x-ray diffraction data of liquid $FeO–Fe_2O_3$[9] and $CaO–FeO–Fe_2O_3$ close to the eutectic composition.[12] In these studies, the Fe–O coordination numbers varied from 4.5 to 5 over the region FeO to Fe_2O_3. Here, we compare new structural melt data on the $BaO–FeO–Fe_2O_3$ and $SrO–FeO–Fe_2O_3$ systems (at the composition $43MO–57FeO_X$, where M = Ca, Sr, Ba) to the density and viscosity as a function of oxygen partial pressure. For an eightfold alkaline earth-oxygen coordination environment in the crystalline forms, the effective M–O bond lengths correspond to 2.82 Å (Ba^{2+}) > 2.66 Å (Sr^{2+}) > 2.52 Å (Ca^{2+}) assuming sixfold O^{2-}.[13] Investigating the effect of metal ion size and relative field strengths in the high temperature melts as a function of fugacity, we find increasing nano-segregation of the Fe–O network structure under more reducing conditions. Using concepts typically associated with silicate melts, we analyze the oxygen connectivity of these model structures.

II. METHODS

Our aerodynamic levitation and high-energy x-ray diffraction experiments have been described in detail previously.[9,14] Here, high purity Fe_2O_3 (99.995%, Sigma-Aldrich), $SrCO_3$ (99.995%, Sigma-Aldrich), and $BaCO_3$ (99.999%, Sigma-Aldrich) powders were weighed and ball milled to create well-mixed batches. The resulting material was calcined and fused by laser heating in a water-cooled copper hearth that both melted and homogenized the components. Beads of ca. 3 mm diameter were levitated in a gas stream using a conical nozzle aerodynamic levitator. Heating was achieved using a 400W CO_2 laser (Synrad Firestar i401) and the temperature of the droplet surface was measured using a 0.9 μm wavelength optical pyrometer (Chino IR-CAS). The oxygen partial pressure, $p(O_2)$, was controlled using five different redox gas mixtures: 5%(99CO:CO_2):95%Ar, 5%(CO:CO_2):95%Ar, 5%CO_2:95%Ar, 0.1%O_2:99.9%Ar, and O_2. The $p(O_2)$ values for the high temperature melts were calculated using the procedure described by Fegley,[15] based on the surface temperature of the droplets. In our previous studies on $43CaO–57FeO_X$, the compositions of the liquids, given by the $Fe^{3+}/\Sigma Fe$ ratio, were calculated using Eq. (12) from Jayasuriya *et al.*[16] For $43BaO–57FeO_X$, the Fe^{3+}/Fe^{2+} ratio was determined from Eq. (1) and the measurements of Hara *et al.*[17] However, no such data exist for $SrO–FeO_X$. To determine the $Fe^{3+}/\Sigma Fe$ ratio for our $43SrO–57FeO_X$ melt, an activity scaling method was used based on the electrochemical measurements of Iwase *et al.*[18] (see Sec. II A for details). The validity of the activity scaling method was verified by comparing the known Fe–O activities in CaO and BaO melts, and the method was estimated to be accurate to within ±10% (supplementary material). As an additional check, the $Fe^{3+}/\Sigma Fe$ ratio for $43SrO–57FeO_X$ melt was also calculated in *FactSage*,[19] based on a CALPHAD assessment of the entire system using the thermodynamic data reported by Jantzen *et al.*[20] The results are shown in Fig. 1(a). For the sake of brevity, those samples measured in an oxygen environment will be referred to as $MO–Fe_2O_3$ (since $Fe^{3+}/\Sigma Fe > 85\%$) and those in the most reducing gas denoted MO–FeO (where $Fe^{3+}/\Sigma Fe < 15\%$).

High-energy x-ray diffraction experiments were carried out on beamline 6-ID-D at the Advanced Photon Source (Argonne, IL, USA) using an incident x-ray beam energy of 100.4 keV.[21] The scattered intensity was measured using a Perkin Elmer XRD1621 area detector over a Q range of 0.5–25.0 $Å^{-1}$. The x-ray beam was aligned to the top 200 μm of the ∼50 mg levitated droplet in conjunction with the laser beam and pyrometer. X-ray diffraction patterns were collected in short 40 s bursts, in ∼100 K steps decreasing from 1973 K, to avoid mass losses of more than a few percent due to evaporation.[9,12] The software *Fit2D*[22] was used to reduce the two-dimensional scattered x-ray data arising just from the top half of the Debye–Scherrer cone, in order to avoid self-attenuation corrections through the bottom of the sample. The x-ray total structure factor S(Q) and corresponding differential pair-distribution function D(r) were obtained using the software *PDFgetX2*.[23] From the measured x-ray pair distribution function, the atomic number densities for both the Ba and Sr melts were found to be constant with pO_2, based on the consistent slope between datasets in the low-r region (below the shortest bond distance distribution) of the x-ray D(r) (See Ref. 24, also see the supplementary material). The consequence of this is a slight rise in the mass density under more reducing conditions as shown in Fig. 1(b).

A. Fe^{3+}/Fe^{2+} ratio in $SrO–FeO_X$ melts from the activity scaling model

Hara *et al.*[17] have shown that the equilibrium reaction between iron oxide-based melts $MO–FeO_X$ and the gas phase can be written as

$$FeO_{1.5}(melt) = FeO(melt) + \frac{1}{4}O_2(gas), \tag{1}$$

where the equilibrium constant K_1 can be defined as

$$K_1 = \frac{a_{FeO}}{a_{FeO1.5}} pO_2^{1/4} = \frac{\gamma_{FeO} X_{FeO}}{\gamma_{FeO1.5} X_{FeO1.5}} pO_2^{1/4}, \tag{2}$$

where pO_2 is the oxygen partial pressure, γ is the activity coefficient, X is the molar fraction, and a is the activity of each component, FeO or $FeO_{1.5}$. Furthermore, the activity coefficient ratio can be directly related to the Fe^{3+}/Fe^{2+} ratio through

$$\frac{Fe^{3+}}{Fe^{2+}} = \frac{\gamma_{FeO1.5}}{\gamma_{FeO}} \frac{a_{FeO}}{a_{FeO1.5}}. \tag{3}$$

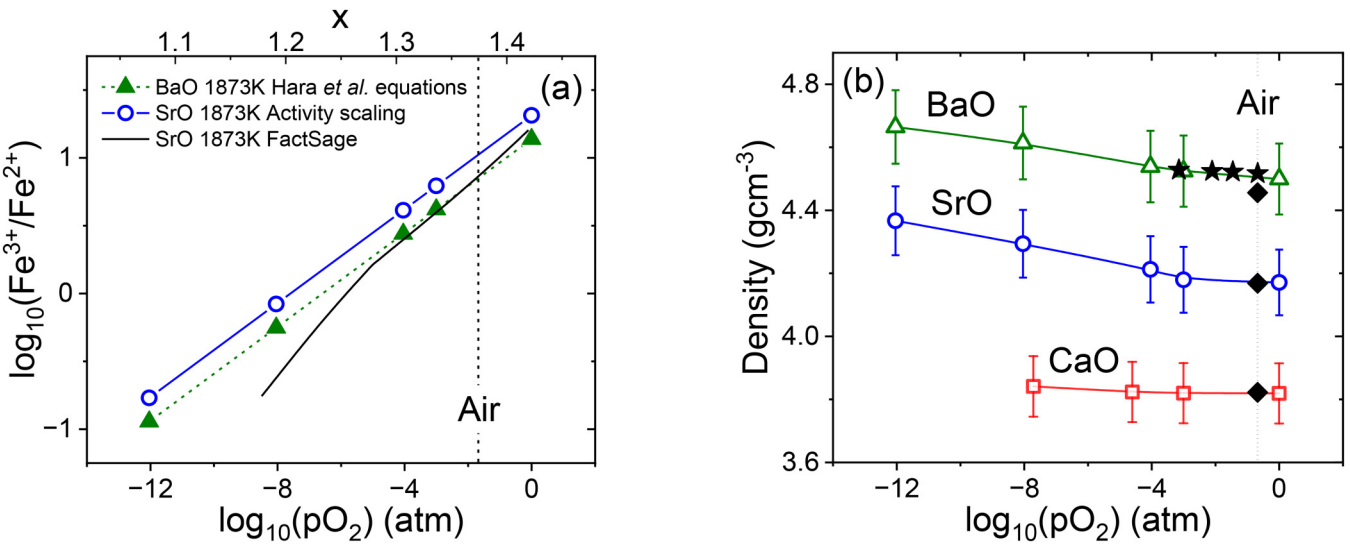

FIG. 1. (a) The Fe^{3+}/Fe^{2+} ratio in 43MO–57FeO_X melts as a function of oxygen partial pressure in different gas environments as a function of temperature or FeO_X. (b) Densities of 43MO–57FeO_X samples, where M = Ba (triangles), M = Sr (circles), and M = Ca (squares) as a function of oxygen partial pressure consistent with the x-ray data, compared to the MO–Fe_2O_3 data of Sumita *et al.*[1] (diamonds) and BaO–FeO–Fe_2O_3 data of Hara *et al.*[17] (Table II, stars).

For the case of BaO–FeO_X melts, Hara *et al.*[17] have measured the relation between Fe^{3+}/Fe^{2+} and pO_2 at a temperature of 1773K. Iwase *et al.*[18] have expressed the Fe_yO activity coefficients for Ca, Sr, and Ba iron oxide melts as linear functions using a solution model, to give the following equations:

$$\frac{\log \gamma_{Fe_yO}}{\left(1 - X_{Fe_yO}\right)^2} = -2.30X_{CaO} + 0.50, \tag{4}$$

$$\frac{\log \gamma_{Fe_yO}}{\left(1 - X_{Fe_yO}\right)^2} = -9.01X_{SrO} + 1.47, \tag{5}$$

$$\frac{\log \gamma_{Fe_yO}}{\left(1 - X_{Fe_yO}\right)^2} = -10.55X_{BaO} + 1.66. \tag{6}$$

The activity of Fe_yO for Sr can be approximated by a linear scaling factor when compared to the activity of Fe_yO for Ba, using data from Tables 2 and 3 from Iwase *et al.*,[18] such that $a_{Fe_yO}(BaO) = 0.92\ a_{Fe_yO}(SrO)$. By combining Eqs. (3), (5), and (6) for our case where the mole fraction $X_{FeyO} = 0.57$, we find

$$Fe^{3+}/Fe^{2+}(SrO) = 0.89\ Fe^{3+}/Fe^{2+}(BaO). \tag{7}$$

Our diffraction experiments were conducted in five redox gas mixtures: 5%(99CO:CO_2):95%Ar, 5%(CO:CO_2):95%Ar, 5%CO_2:95%Ar, 0.1%O_2:99.9%Ar, O_2 (Shi *et al.*[9]). Consequently, neglecting the temperature dependence, we find the Fe^{3+}/Fe^{2+} ratios for 43SrO–57FeO_X and 43BaO–57FeO_X melts as a function of gas composition shown in Table I.

B. EPSR modeling

Atomistic empirical potential structure refinement (EPSR) is a Monte Carlo approach to modeling liquid x-ray and neutron diffraction data,[25,26] whereby initial "reference" starting pair potentials and effective Coulomb charges are perturbed in order to obtain agreement between model and experimental structure factors. This ensures that the starting configuration is close to the final one, and

TABLE I. The Fe^{3+}/Fe^{2+} ratio and $\%Fe^{3+}$ in 43BaO–57FeO_X (measured) and 43SrO–57FeO_X melts at 1873 K as a function of gas composition.

		43BaO–57Fe_XO		43SrO–57Fe_XO	
Gas composition	$Log_{10}(pO_2)$ (atm)	Fe^{3+}/Fe^{2+}	$\%Fe^{3+}$	Fe^{3+}/Fe^{2+}	$\%Fe^{3+}$
5%(99CO:CO_2):95%Ar	−12.0	0.114	10.2	0.170	14.5
5%(CO:CO_2):95%Ar	−8.0	0.560	35.9	0.836	45.5
5%CO_2:95%Ar	−4.0	2.75	73.4	4.11	80.4
0.1%O_2:99.9%Ar	−3.0	4.17	80.6	6.23	86.2
O_2	0.0	13.8	93.2	20.6	95.4

TABLE II. Starting EPSR Lennard-Jones reference potentials.

Atom	Effective charge (e)	ε (kJ/mole)	σ (Å)
Ba^{2+}	+1.0	0.3000	3.00
Sr^{2+}	+1.0	0.3500	2.60
Fe^{3+}	+1.5	0.1500	1.70
Fe^{2+}	+1.0	0.1500	1.65
O^{2-}	−1.0	0.1625	3.60

only slight changes to the inter-atomic potential need to be made during the empirical potential adjustment process to improve the fit with the data. EPSR models of $43BaO–57FeO_X$ and $43SrO–57FeO_X$ melts were fitted against the high-energy x-ray diffraction data. EPSR models of 6000 atoms in a cubic box were constructed using the compositions determined from the $Fe^{3+}/\Sigma Fe$ ratio. The reference potentials for Fe^{2+}, Fe^{3+}, and O^{2-} were based on previous studies,[9] and those for Ba and Sr were scaled relative to their effective ionic radii,[13] see Table II. Interactions between like atoms (Ba–Ba, Sr–Sr, Fe–Fe, O–O) are determined using the standard Lorentz–Berthelot mixing rules. Examples of the EPSR results with and without the empirical potential are shown in Fig. S1 in the supplementary material. The atomic number densities were fixed to those reported by Sumita *et al.*[1] and Hara *et al.*[27] (leading to cubic box edge lengths of ∼5 nm see discussion section for further details). Monte Carlo ensembles were collected for 2000 configurations. The EPSR fits to the measured x-ray data are shown in Figs. S2 and S3 in the supplementary material, with example D(r) shown in Fig. 2.

The EPSR approach does suffer from the "uniqueness" problem, such that different 3D atomic configurations could equally well reproduce the measured S(Q) and G(r).[28] However, it has the benefit of accurately reproducing the experimental data, which is not currently possible using classical molecular dynamics potentials. In our previous paper on liquid FeO_X, we surveyed seven different molecular dynamics interatomic Fe^{2+} potentials and compared the results to our PDF for liquid FeO.[9] The results showed significant inadequacies for all existing MD potentials.

It is important to note that the EPSR simulations required additional minimum distance constraints to prevent unreasonably short M–O bonds appearing. The minimum distance constraints for M–M/Fe correlations were set to $r_{min} = 2.3$ Å, Ba–O correlations to $r_{min} = 2.20$ Å, and Sr–O correlations to $r_{min} = 2.15$ Å. Models with larger σ also led to similar results as reported here.

III. RESULTS

The total x-ray pair distribution functions of $MO–Fe_2O_3$ melts are shown in Fig. 2, where the first peak is mostly due to overlapping Fe^{3+}–O and Fe^{2+}–O bonds. In the measured x-ray D(r), the first peak position increases from 1.92(1) to 1.95(1) Å in more reducing atmospheres, consistent with the average Fe^{2+}–O bond lengths being slightly longer than Fe^{3+}–O.[9] Overall, D(r) are composed of 10 x-ray weighted partial pair distribution functions: Fe^{2+}–Fe^{2+}, Fe^{2+}–Fe^{3+}, Fe^{3+}–Fe^{3+}, Fe^{2+}–O, Fe^{3+}–O, Fe^{2+}–M, Fe^{3+}–M, M–O, M–M, and O–O correlations. Representative partial pair distribution functions are shown in Fig. 3 for the intermediate (in terms of redox) $43MO–57FeO_{1.33}$ melt systems. The Sr–O and Ba–O first coordination shells are highly distorted with typical

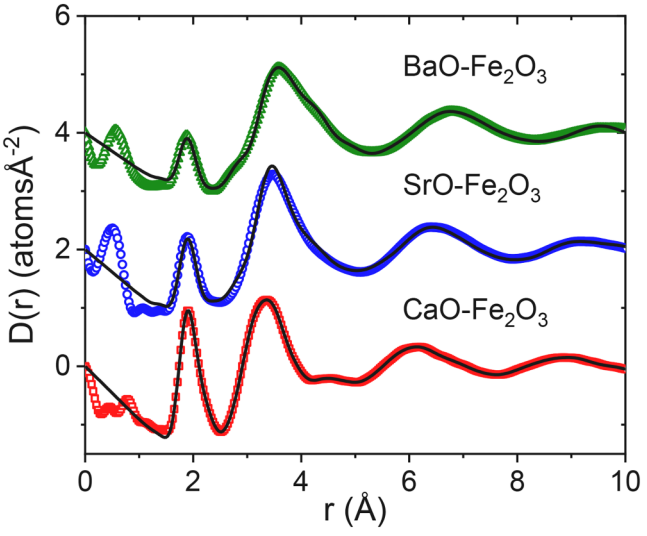

FIG. 2. X-ray differential distribution functions $D(r) = 4\pi\rho r[G(r)-1]$ (symbols) and EPSR fits (lines) of samples measured in oxygen at 1873 K.

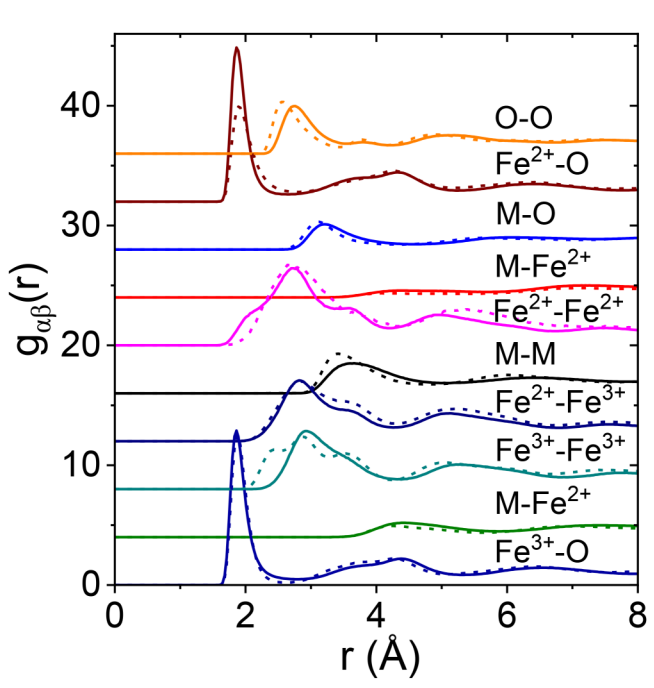

FIG. 3. Example partial pair distribution functions for $43MO–57Fe_2O_3$ at 1873 K, where the M = Ba melt is shown as solid lines and the M = Sr melt is shown as dashed lines when exposed to the intermediate 5%($CO:CO_2$):95%Ar gas environment.

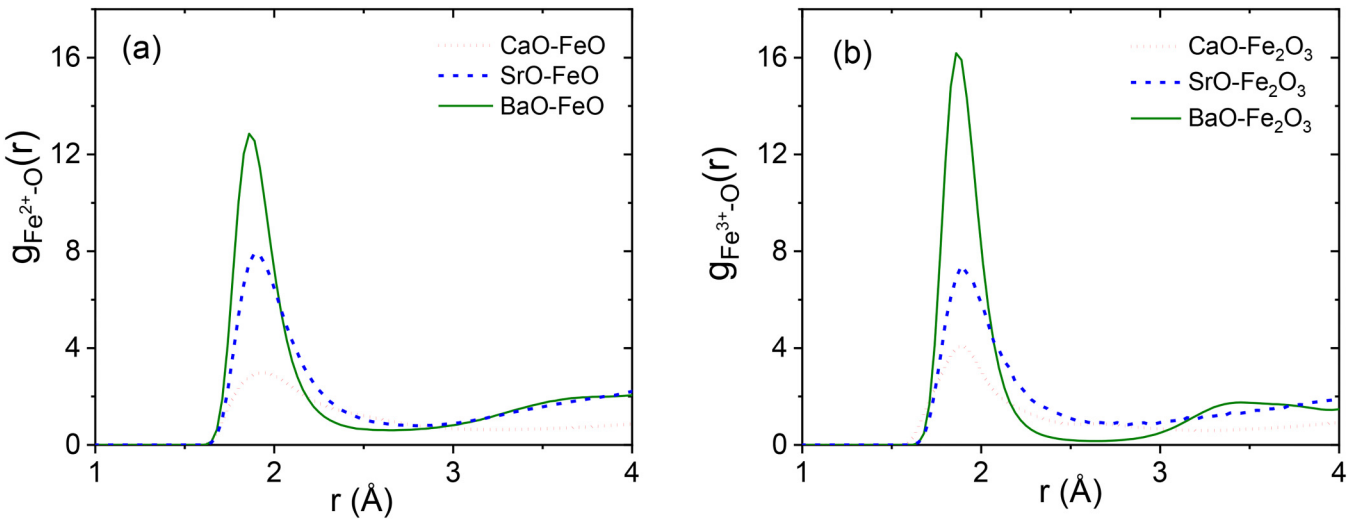

FIG. 4. Iron oxygen EPSR partial pair distribution functions: (a) Fe^{2+}–O in 5%($CO:CO_2$):95%Ar gas for BaO, SrO, and CaO, compared to (b) Fe^{3+}–O in O_2 gas.

bond distances of 3.1 and 3.2 Å, respectively. These values are both slightly longer than those observed in the low temperature ferrite crystals $r_{Sr-O} \sim 2.8$ Å[5] and $r_{Ba-O} = 2.9–3.0$ Å,[29,30] and much longer than predicted by the effective ionic radii $r_{Sr-O} \sim 2.66$ and $r_{Ba-O} \sim 2.82$ Å for eightfold polyhedra.[13]

The local Fe^{2+}–O and Fe^{3+}–O environments are shown in Fig. 4 for the most reducing and the most oxidizing conditions. In both cases, the first Fe–O shell is sharpest for the Ba system, becoming progressively broader and extending to longer distances as the metal ion size is decreased to Sr and Ca. The corresponding running coordination numbers are shown in Fig. S5 in the supplementary material.

IV. DISCUSSION

In the iron and steelmaking process, the ferrite liquid properties, chemical reaction rates, and reaction spontaneity are strongly influenced by the Fe_yO activity, which depends on the relative Fe–O bond strengths and coordination environments.[12] In the solid state (before melting), many of the $BaFeO_X$ and $SrFeO_X$ crystal structures are isostructural. Monoferrite $BaFe_2O_4$ contains only FeO_4,[29] while $BaFe_4O_7$ contains both FeO_4 tetrahedra and FeO_6 octahedra.[30] Crystalline $SrFe_{12}O_{19}$ contains FeO_4, FeO_6 and bypyramidal FeO_5 arising from fast diffusional motion between two pseudo-tetrahedral sites.[3] Crystal structures in the perovskite series $SrFeO_{2.5-3}$ contain Fe^{3+} ions in FeO_4 and FeO_6 sites, as well as tetravalent (Fe^{4+}) in fivefold pyramidal units.[4–6] The individual coordination numbers in this study were determined by the average of integrating out to the first minima in $g_{FeO}(r)$ and the first minima in $rg_{FeO}(r)$ beyond the first peak. The total Fe–O (Fe^{2+}–O + Fe^{3+}–O) coordination number for both $43MO–57Fe_2O_3$ (M = Ba, Sr) systems shown in Fig. 5 are very similar at $n_{Fe-O} \sim 5.7$ [see Fig. 5(a)]. However, n_{Fe-O} decreases linearly with decreasing $Fe^{3+}/\Sigma Fe$ to 4.9 for the Ba system, but increases linearly to 6.3 for Sr over the same range.

Given that the field strength of an ion is the charge divided by its ionic radius, the ion-oxygen parameter can be defined that describes the Coulombic force between the cation and oxygen anion, where $I = 2z/(r_C + r_O)^2$ and z is the valency of the cation and 2 is the valency of oxygen. For the ions in this study, the Coulombic force (and field strength) increases with ion size[31] such that

$$I = 1.5(Fe^{3+}) > 0.87(Fe^{2+}) > 0.7(Ca^{2+}) > 0.56(Sr^{2+}) > 0.50(Ba^{2+}).$$

Large values of I indicate a relatively strong interaction between the metal cation and oxygen, and smaller values correspond to weaker interactions. This ranking is consistent with the heights of the cation–oxygen peaks in Fig. 3, where Fe^{3+}–O partial pair distribution function has the sharpest nearest neighbor peak, followed by Fe^{2+}–O. It is also reflected in the ionicity of bonding, which can be estimated by the difference in electronegativity χ of the elements,[31] $i = 1 - \exp[-(\chi_\alpha - \chi_\beta)^2/4]$. Here, lower field strength Ba^{2+}–O bonds tend to be much more ionic than Sr^{2+}–O bonds, which have a similar character to the Fe ions, such that

$$\text{Ionicity of bonding, } i(\%):82(Ba^{2+}) > 79(Ca^{2+}) > 51(Fe^{2+}) > 49(Sr^{2+}) > 47(Fe^{3+}).$$

The Ba–O coordination environment in crystal structures of the $BaFeO_X$ system can take on a range of values between 7 and 12. Monoferrite has two environments BaO_7 and BaO_{11},[29] hexaferrite contains BaO_{12} with both long and short bonds,[3] and $BaFe_4O_7$ has BaO_9 polyhedra with two distinct Ba–O distances.[30] Our EPSR models yield average metal–oxygen coordination numbers of $n_{MO} = 8.4$ in $43MO–57Fe_2O_3$ compared to $n_{CaO} = 5.4$ in $43CaO–57Fe_2O_3$.[12] The Sr–O coordination remains relatively

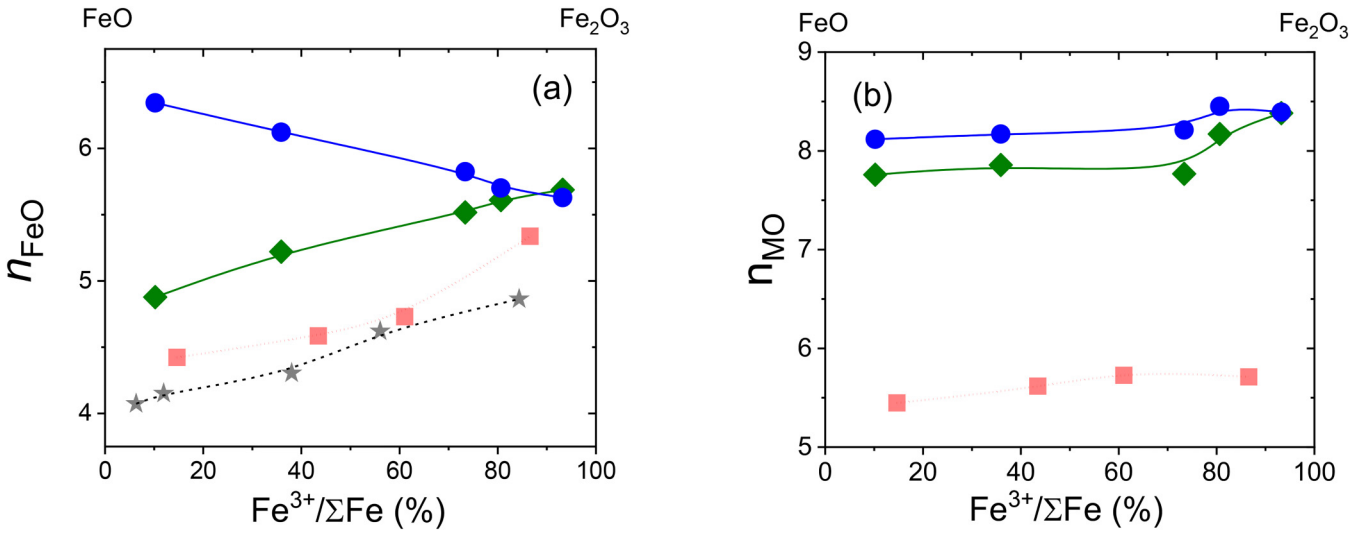

FIG. 5. Average (a) iron-oxygen and (b) metal oxygen coordination numbers from our EPSR models for $BaO–FeO_X$ (green diamonds), $SrO–FeO_X$ (blue circles) compared to $CaO–FeO_X$ (red squares) and pure FeO_X (stars).

constant with decreasing Fe^{3+}, but the Ba–O coordination decreases slightly, by up to ~0.6, at lower Fe^{3+}.

We have previously found the total Fe–O coordination numbers (n_{FeO}) for $CaO–FeO_X$ melts increase with increasing $Fe^{3+}/\Sigma Fe$ ratio,[12] see Fig. 5. A similar behavior is found for the total Fe–O coordination in $BaO–FeO_X$ melts, but the opposite trend found for $SrO–FeO_X$ melts. To investigate further, we show the trends for Fe^{3+}-O and Fe^{2+}–O coordination numbers with $Fe^{3+}/\Sigma Fe$ ratio in Fig. 6. Here, we find the ferric coordination number to be $n_{Fe3+O} \sim 5.7$ for both $43MO–57Fe_2O_3$ (M = Ba,Sr) liquids, but the behavior diverges under reducing conditions toward 5.2 for Ba and to 6.3 for Sr. More stark differences appear in the ferrous coordination number between the two alkaline earth liquids, with n_{Fe3+O} essentially constant at ~5.0 across $Fe^{3+}/\Sigma Fe$ for Ba, while for Sr, the numbers are offset to $n_{Fe3+O} = 5.6$ at $43SrO–57Fe_2O_3$ and rising to 6.3 at 43SrO–57FeO.

These results are also reflected in the distributions of n-fold Fe^{2+}–O and Fe^{3+}–O coordination species in Fig. 7. Our EPSR

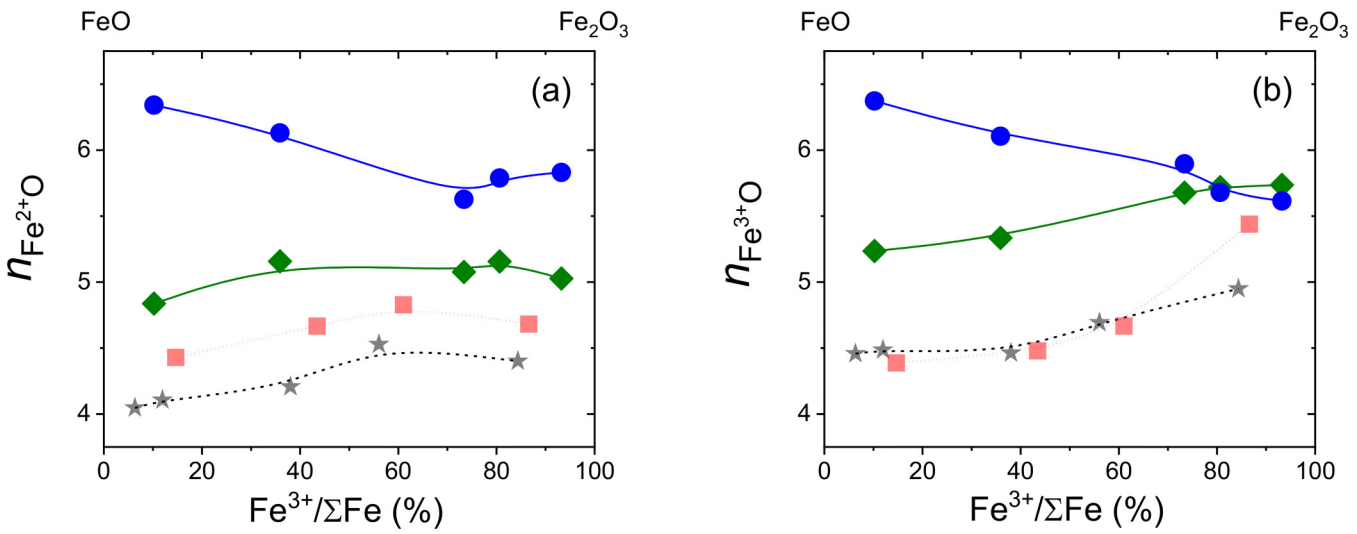

FIG. 6. Average iron oxygen coordination numbers from our EPSR models for (a) $Fe^{2+}O$ and (b) $Fe^{3+}O$. $BaO–FeO_X$ (green diamonds), $SrO–FeO_X$ (blue circles) compared to $CaO–FeO_X$ (red squares) and pure molten FeO_X (stars).

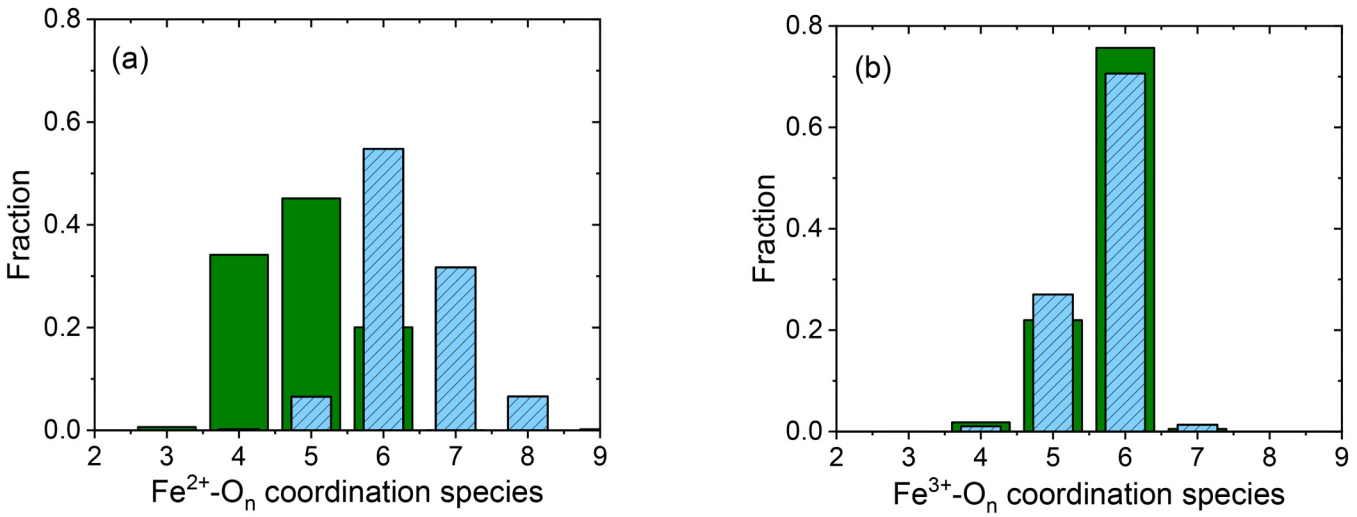

FIG. 7. Distribution of BaO_m (solid green) and SrO_n (shaded blue) coordination species for (a) $Fe^{2+}O$ in MO–FeO liquids and (b) $Fe^{3+}O$ in for MO–Fe_2O_3 liquids.

models show that Fe^{3+} ions are predominantly five and sixfold coordinated by oxygen atoms under oxidizing conditions for both Ba and Sr liquids. Under reducing conditions, Fe^{2+} ions are mainly four, five, and sixfold for Ba, but six and sevenfold for Sr melts. In general, low Fe–O coordination numbers, i.e., $n_{FeO} < 6$, have been found experimentally in many iron oxide melts using scattering and spectroscopy methods. For example, Alderman *et al.* found $n_{FeO} = 4.4$ in Fayalite,[32] Shi *et al.* obtained $n_{FeO} = 4–5$ in FeO_X[9] and $43CaO–57FeO_X$,[12] and Drewitt *et al.* measured $n_{Fe2+O} = 3.3$ in $FeAl_2O_4$.[33] Similarly, first principles molecular dynamics (MD) have predicted $n_{Fe2+O} = 4.5$ in liquid $FeMg_3O_4$[34] and $n_{Fe-O} = 3.7$ in pyrolitic silicate melts.[35] In addition, the *ab initio* MD calculations of Ghosh and Karki[36] have predicted undercoordinated $n_{Fe2+O} = 3.8$ and $n_{Fe3+O} = 4.1$ for high-spin and $n_{Fe2+O} = 3.3$ and $n_{Fe3+O} = 3.7$ for low-spin in $MgSiO_3$ melt at 3000 K.

A significant degree of nanoscale heterogeneity is observed in the EPSR models achieved via the edge-sharing iron polyhedra. This increases under more reducing conditions as channels of BaO_X polyhedra become segregated from the FeO_X edge-shared network (Fig. 8). This is expected from a thermodynamic perspective, since reducing conditions at some point favor a two-phase MO(solid) + FeO-rich melt equilibrium as a result of the free energy minimization of the system.

Finally, we consider the relationship between the presence of various local atomic polyhedral units and the thermodynamic and electronic properties of liquid iron oxide slags. Hara *et al.*[17] have developed equations that reproduce the densities of $BaO–FeO_X$ melts to within ±0.7% and were used to set up the oxygen-rich EPSR models as described in Sec. II and shown in Fig. 1(b). Sumita *et al.*[1] have measured the densities, viscosities, and electrical conductivities of melts in the MO–FeO_X systems under controlled partial pressures from the liquidus temperature to 1873 K. For $43MO–57Fe_2O_3$ liquids, the viscosities are found to range from

$$\eta = 27.1(\mathrm{Ba}) > 19.2(\mathrm{Sr}) > 15.8(\mathrm{Ca})\ \mathrm{mPa\ s\ at\ T} = 1773\ \mathrm{K}.$$

For the electrical conductivity at the $45MO–57Fe_2O_3$ composition,

$$\sigma = 22.9(\mathrm{Sr}) > 18.3(\mathrm{Ca}) > 12.8(\mathrm{Ba})\mathrm{S/m\ at\ T} = 1773\ \mathrm{K}.$$

In binary ferrite melts, it has been suggested that the atomic fraction of $Fe^{3+}O_4$ is the main factor in determining the viscosity due to the polymerization of the tetrahedral network and the abundance of FeO_6 units the main factor in affecting the electrical conductivity.[1]

Sumita *et al.*[1] interpreted the viscosity and electrical conductivity behavior in terms of the Fe^{3+} coordination model. The $Fe^{3+}(4–6)$ model assumes that all Fe^{2+} is sixfold and (i) Fe_2O_3 consists of 100% sixfold $Fe^{3+}(6)$, which decreases linearly with increasing FeO and are replaced by fourfold $Fe^{3+}(4)$ ions (ii) the main factor controlling the viscosity of the melts is the $Fe^{3+}(4)$ content. (iii) The electrical conductivity is determined by the concentration of the charge carriers (c_α) for $\alpha = M^{2+}$, $Fe^{2+}(6)$, and $Fe^{3+}(6)$, which contribute depending on their ionic radii r_α because the mobility of the ions is assumed to be inversely proportional to the ionic radius. Hence,

$$\log\sigma \propto \sum_\alpha \frac{\mathrm{valence}}{r_\alpha} c_\alpha = \frac{2}{r_M} c_M + \frac{2}{r_{Fe2+}} c_{Fe2+(6)} + \frac{3}{r_{Fe3+}} c_{Fe3+(6)}. \quad (8)$$

From our EPSR models, this formula yields values of 102.7 for $BaO–Fe_2O_3$ and 110.1 for $SrO–Fe_2O_3$ melts in air, consistent with the trend in electrical conductivity measurements.

However, given the discussion above on the substantial fivefold coordination of Fe–O species in iron oxide melts, it is

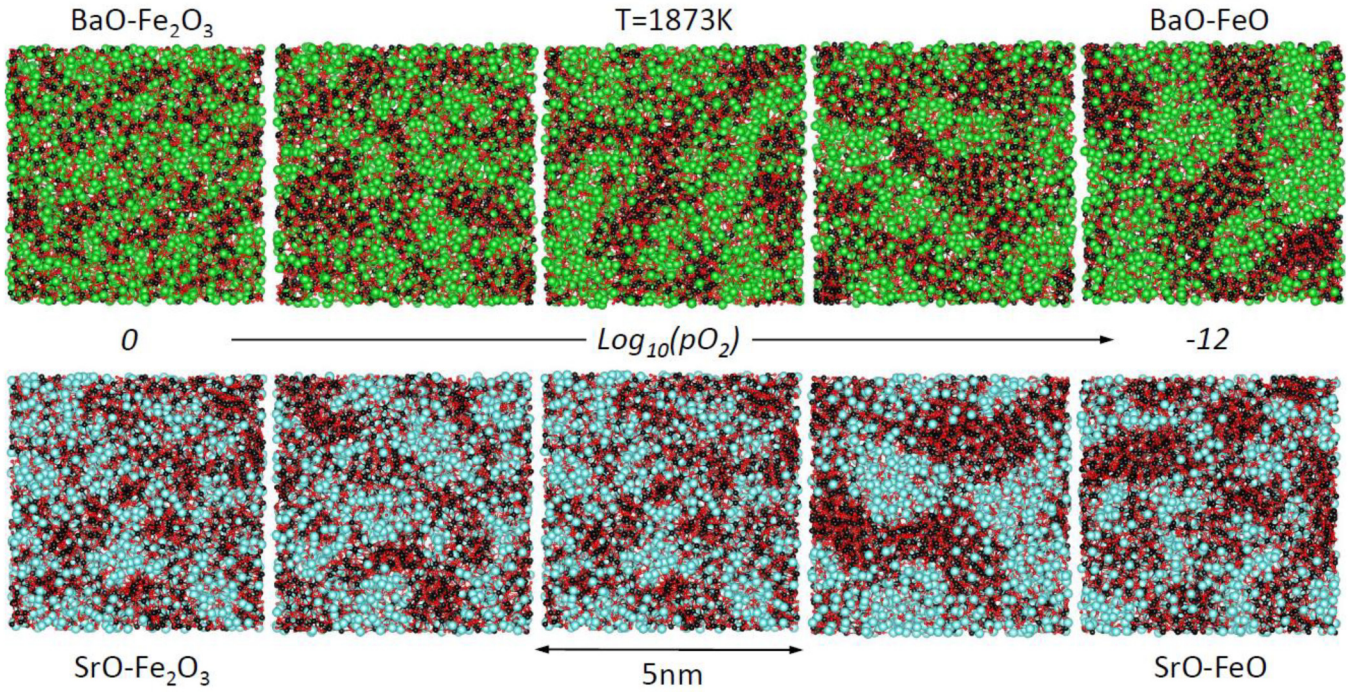

FIG. 8. Increasing nano-segregation of $FeO_{4,5,6}$ and $Ba/SrO_{7,8}$ polyhedra under increasingly reducing conditions. Ba atoms are shown in green, Sr atoms are shown in blue, Fe atoms are shown in black, and O atoms are shown in red.

unsurprising that the Fe^{3+}(4–6) model does not fit the viscosity relation for $43MO–57Fe_2O_3$ liquids. Among the different types of viscosity models used to describe silicate slags some of the more sophisticated involve the consideration of the different types of oxygen ions within the liquid network structure.[37,38] For example, López-Rodríguez *et al.*[39] suggest that in binary silicate–metal oxide systems, viscosity can be expressed as $\log\eta = A + B/T + C \cdot BO$ for Arrhenius liquids, where BO refers to bridging oxygens. In our case, since no silica is present, we take a more generalized view of the three different types of oxygen atoms present in the liquid, i.e., (i) bridging oxygens (BOs) between tetrahedral units (ii) non-bridging oxygens (NBOs) associated with tetrahedral units and (iii) free oxygens not bonded to any tetrahedra. In addition, on the basis of first principles molecular dynamics simulations on $MgSiO_3$ melts, it has been suggested that the difference in viscosity among the different valence states of Fe is not significant.[36] We, therefore, also assume that the viscosity in our alkaline earth liquids under reducing conditions will depend on the sum of at. % Fe^{2+}(tetra) $+Fe^{3+}$(tetra) rather than just at. % Fe^{3+}(tetra). Consequently, a high degree of FeO_4 with many bridging oxygens would lead to a highly polymerized liquid network with a high viscosity, whereas FeO_5 and FeO_6 would be responsible for the depolymerization of slag networks resulting in a decrease in slag viscosity. The oxygen connectivity for our $MO–FeO_X$ liquid EPSR models were calculated using the *Atomes* software.[40] The results shown in Fig. 9 indicate slightly higher percentages of BOs (7%) and NBOs (9%)

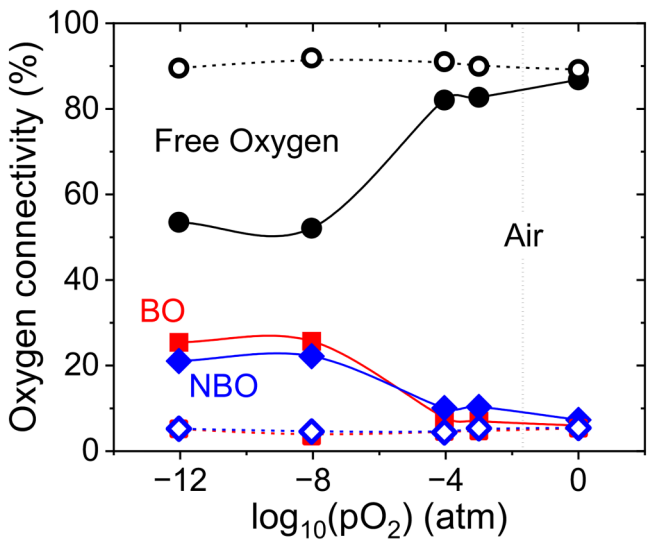

FIG. 9. Oxygen connectivity as a function of oxygen partial pressure in the Ba (closed symbols and solid lines) and Sr (open symbols and dashed lines) melts at 1873 K, with bridging oxygens (BOs, red squares), nonbridging oxygens (NBOs, blue diamonds), and free oxygens (black circles) using a cut-off of 2.5 Å.

in $BaO–Fe_2O_3$ melts in comparison to values of BOs (5%) and NBOs (5%) in $SrO–Fe_2O_3$ melts in air. The number of BOs and NBOs increases under reducing conditions for Ba-ferrite liquids indicating that viscosity increases. Conversely, we find the majority of oxygen atoms in these liquids are free oxygens, which remain constant in SrO–FeO liquids under reducing conditions, but decrease substantially in reduced oxygen BaO–FeO liquids. Generally, since network forming (Fe^{3+}) cations are acidic in nature and network breakers (M) are basic,[41] the high number of free oxygens available in oxygen-rich environments indicates a higher basicity and reactivity of the melt.[42]

V. FUTURE STUDIES

In Sr–Fe–O and Ba–Fe–O liquids studied in this work, it has been determined that most oxygen ions are not bonded to FeO_4 tetrahedra. The prevalence of free oxygen suggests that oxygen exchange dynamics with gaseous surroundings may play a determinative role in controlling melt properties that are correlated with molecular structure such as density, viscosity, and electrical conductivity. Oxygen partial pressure was varied over 12 orders of magnitude by use of gaseous fugacity buffers in this work; however, further increases in oxygen partial pressure to stabilize metal cations in high oxidation states whose field strengths may modify the distributions of local coordination numbers so as to significantly influence melt structure–property relationships will require system pressurization.[43,44] Toward this goal, future experiments will utilize a hyperbaric levitator[45] to conduct structure measurements of fully trivalent iron oxide liquids at an oxygen partial pressure of 100 bar at a temperature of 1873 K. The effect in Fig. 1(a), will be to expand the accessible range of $Fe^{3+}/\Sigma Fe$ and is expected to permit congruent melting behavior of many ferrite compositions of technological interest, especially in Ba–Fe–O systems whose weaker metal–oxygen bonding leads to greater sensitivity of local coordination as a function of oxygen fugacity as shown in Figs. 5(b) and 9. Notably, as pressure increases from 1 to 100 bar, oxygen undergoes a supercritical fluid transition that may provide additional experimental benefits as discussed by Phelan *et al.*.[46] In addition to temperature and composition, the effect of partial pressure of reactive species (i.e., oxygen for the case of molten oxides) on chemical potential is key to understanding stability of system constituents. Thus, the importance of extended redox regimes to fully capture structural evolution of oxide systems from the melt to the crystalline state cannot be understated.

SUPPLEMENTARY MATERIAL

See the supplementary material for EPSR model potential parameters, model fits to diffraction data, metal–oxygen coordination numbers, and the Fe^{3+}/Fe^{2+} ratio from the activity scaling model.

ACKNOWLEDGMENTS

Dr. Gustavo Costa is thanked for useful discussions on the Fe^{2+}/Fe^{3+} ratio. This work was supported as part of the Center for Steel Electrification by Electrosynthesis (C-STEEL), an Energy Earthshot Research Center funded by the U.S. Department of Energy, Office of Science, Basic Energy Sciences (BES) and Advanced Scientific Computing Research (ASCR). This research used resources of the Advanced Photon Source, the U.S. Department of Energy (DOE) Office of Science User Facility operated for the DOE Office of Science by Argonne National Laboratory under Contract No. DE-AC02-06CH11357. This work was partially funded under DOE Grant Nos. DE-SC0015241 and DE-SC0018601. This work was supported by the National Key Basic Research Program of China (Grant No. 2020YFA0406101). C.S. gratefully acknowledges financial support from the China Scholarship Council (CSC No. 201706890053).

AUTHOR DECLARATIONS

Conflict of Interest

The authors have no conflicts to disclose.

Author Contributions

C. J. Benmore: Conceptualization (equal); Data curation (equal); Formal analysis (equal); Funding acquisition (equal); Investigation (equal); Methodology (equal); Project administration (equal); Validation (equal); Writing – original draft (equal); Writing – review & editing (equal). **C. Shi:** Conceptualization (equal); Data curation (equal); Formal analysis (equal); Investigation (equal); Methodology (equal); Writing – review & editing (equal). **O. L. G. Alderman:** Conceptualization (equal); Formal analysis (equal); Methodology (equal); Validation (equal); Writing – review & editing (equal). **J. P. Harvey:** Formal analysis (equal); Methodology (equal); Validation (equal); Writing – review & editing (equal). **D. Lipke:** Investigation (equal); Methodology (equal); Writing – review & editing (equal). **J. K. R. Weber:** Conceptualization (equal); Data curation (equal); Funding acquisition (equal); Writing – review & editing (equal).

DATA AVAILABILITY

The data that support the findings of this study are available from the corresponding author upon reasonable request.

REFERENCES

[1]S. Sumita, K. Morinaga, and T. Yanagase, "Physical properties and structure of binary ferrite melts," Trans. Jpn Inst. Met. **24**(1), 35–41 (1983).
[2]T. Nagasaka, Y. Iguchi, and S. Ban-Ya, "Effect of additives on the rate of reduction of liquid iron oxide with CO," Tetsu-To-Hagane/J. Iron Steel Inst. Jpn **75**(1), 74–81 (1989).
[3]X. Obradors, X. Solans, A. Collomb, D. Samaras, J. Rodriguez, M. Pernet, and M. Font-Altaba, "Crystal structure of strontium hexaferrite $SrFe_{12}O_{19}$," J. Solid State Chem. **72**(2), 218–224 (1988).
[4]M. Schmidt, M. Hofmann, and S. J. Campbell, "Magnetic structure of strontium ferrite $Sr_4Fe_4O_{11}$," J. Phys. Condens. Matter **15**(50), 8691 (2003).
[5]J. P. Hodges, S. Short, J. D. Jorgensen, X. Xiong, B. Dabrowski, S. M. Mini, and C. W. Kimball, "Evolution of oxygen-vacancy ordered crystal structures in the perovskite series $Sr_nFe_nO_{3n-1}$ (n=2, 4, 8, and ∞), and the relationship to electronic and magnetic properties," J. Solid State Chem. **151**(2), 190–209 (2000).
[6]M. Takano, T. Okita, N. Nakayama, Y. Bando, Y. Takeda, O. Yamamoto, and J. B. Goodenough, "Dependence of the structure and electronic state of $SrFeO_x$ ($2.5 \leq x \leq 3$) on composition and temperature," J. Solid State Chem. **73**(1), 140–150 (1988).

[7]L. Pargamin, C. H. P. Lupis, and P. A. Flinn, "Mössbauer analysis of the distribution of iron cations in silicate slags," Metall. Trans. **3**(8), 2093–2105 (1972).
[8]M. Hayashi, K. Horita, R. Endo, T. Watanabe, and M. Susa, "Effect of coordination structure of iron ions on iron oxide activities in Na_2O–SiO_2–FeO–Fe_2O_3 melts," Trans. Iron Steel Inst. Japan **59**(10), 1744–1751 (2019).
[9]C. Shi, O. L. G. Alderman, A. Tamalonis, R. Weber, J. You, and C. J. Benmore, "Redox-structure dependence of molten iron oxides," Commun. Mater. **1**(1), 80 (2020).
[10]G. A. Waychunas, G. E. Brown, C. W. Ponader, and W. E. Jackson, "Evidence from X-ray absorption for network-forming Fe^{2+} in molten alkali silicates," Nature **332**(6161), 251–253 (1988).
[11]M. Wilke, "Fe in magma—An overview," Ann. Geophys. **48**(4), 609 (2005).
[12]C. Shi, O. L. G. Alderman, A. Tamalonis, J. K. R. Weber, and C. J. Benmore, "The structure of molten calcium ferrite under various redox conditions," Philos. Trans. Roy. Soc. A **381**(2258), 20220352 (2023).
[13]R. D. Shannon and C. T. Prewitt, "Effective ionic radii in oxides and fluorides," Acta Crystallogr. Sect. B Struct. Crystallogr. Cryst. Chem. **25**(5), 925–946 (1969).
[14]C. J. Benmore and J. K. R. Weber, "Aerodynamic levitation, supercooled liquids and glass formation," Adv. Phys. X **2**(3), 717–736 (2017).
[15]B. Fegley, *Practical Chemical Thermodynamics for Geoscientists* (Academic Press, Boston, 2013).
[16]K. D. Jayasuriya, H. S. C. O'Neill, A. J. Berry, and S. J. Campbell, "A Mössbauer study of the oxidation state of Fe in silicate melts," Am. Mineral. **89**(11–12), 1597–1609 (2004).
[17]S. Hara, K. Irie, D. R. Gaskell, and K. Ogino, "Densities of melts in the FeO-Fe_2O_3-BaO system," Trans. Jpn Inst. Met. **29**(12), 977–989 (1988).
[18]M. Iwase, N. Yamada, E. Ichise, and H. Akizuki, "A thermodynamic study of SrO + Fe_xO and BaO + Fe_xO liquid slags by disposable electrochemical oxygen probes," Arch. Eisenhüttenwesen **55**(9), 415–420 (1984).
[19]C. W. Bale, E. Bélisle, P. Chartrand, S. A. Decterov, G. Eriksson, A. E. Gheribi, K. Hack, I.-H. Jung, Y.-B. Kang, J. Melançon, A. D. Pelton, S. Petersen, C. Robelin, J. Sangster, P. Spencer, and M.-A. Van Ende, "Factsage thermochemical software and databases, 2010–2016," Calphad **54**, 35–53 (2016).
[20]T. Jantzen, S. Petersen, and K. Hack, "Thermodynamic assessment of the Fe–Sr–O system with special attention to the perovskite phase," Chem. Eng. Sci. **211**, 115271 (2020).
[21]L. B. Skinner, C. J. Benmore, and J. B. Parise, "Area detector corrections for high quality synchrotron X-ray structure factor measurements," Nucl. Instrum. Methods Phys. Res. Sect. A **662**(1), 61–70 (2012).
[22]A. P. Hammersley, S. O. Svensson, M. Hanfland, A. N. Fitch, and D. Hausermann, "Two-dimensional detector software: From real detector to idealised image or two-theta scan," High Pressure Res. **14**, 235–248 (1996).
[23]X. Qiu, J. W. Thompson, and S. J. L. Billinge, "PDFgetX2: A GUI-driven program to obtain pair distribution function from X-ray powder diffraction data," J. Appl. Crystallogr. **37**, 678 (2004).
[24]C. J. Benmore, "X-ray and neutron diffraction from glasses and liquids," in *Comprehensive Inorganic Chemistry III*, 3rd ed., edited by J. Reedijk and K. R. Poeppelmeier (Oxford, Elsevier, 2023), Chap. 10.14, pp. 384–424.
[25]A. K. Soper, "Empirical potential Monte Carlo simulation of fluid structure," Chem. Phys. **202**(2), 295–306 (1996).
[26]A. K. Soper, "Joint structure refinement of x-ray and neutron diffraction data on disordered materials: Application to liquid water," J. Phys.: Condens. Matter **19**(33), 335206 (2007).
[27]S. Hara, K. Irie, D. R. Gaskell, and K. Ogino, "Densities of melts in the FeO-Fe_2O_3-CaO and FeO-Fe_2O_3-2CaO·SiO_2 systems," Trans. Jpn Inst. Met. **29**(12), 977–989 (1988).
[28]A. K. Soper, "On the uniqueness of structure extracted from diffraction experiments on liquids and glasses," J. Phys.: Condens. Matter **19**(41), 415108 (2007).
[29]H. Mitsuda, S. Mori, and C. Okazaki, "The crystal structure of barium monoferrite, $BaFe_2O_4$," Acta Crystallogr. Sect. B Struct. Crystallogr. Cryst. Chem. **27**(6), 1263–1269 (1971).
[30]S. Okamoto, S. I. Okamoto, and T. Ito, "The crystal structure of barium diferrite," Acta Crystallogr. Sect. B Struct. Crystallogr. Cryst. Chem. **29**(4), 832–838 (1973).
[31]Y. Waseda and J. M. Toguri, *The Structure and Properties of Oxide Melts: Application of Basic Science to Metallurgical Processing* (World Scientific, 1998).
[32]O. L. G. Alderman, L. Lazareva, M. C. Wilding, C. J. Benmore, S. M. Heald, C. E. Johnson, J. A. Johnson, H.-Y. Hah, S. Sendelbach, A. Tamalonis, L. B. Skinner, J. B. Parise, and J. K. R. Weber, "Local structural variation with oxygen fugacity in Fe_2SiO_{4+x} fayalitic iron silicate melts," Geochim. Cosmochim. Acta **203**, 15–36 (2017).
[33]J. W. E. Drewitt, A. C. Barnes, S. Jahn, R. A. Brooker, L. Hennet, D. R. Neuville, and H. E. Fischer, "Iron coordination in liquid $FeAl_2O_4$," Philos. Trans. R Soc. A **381**(2258), 20220351 (2023).
[34]E. Holmström and L. Stixrude, "Spin crossover in liquid (Mg,Fe)O at extreme conditions," Phys. Rev. B **93**(19), 195142 (2016).
[35]N. V. Solomatova and R. Caracas, "Pressure-induced coordination changes in a pyrolitic silicate melt from *ab initio* molecular dynamics simulations," J. Geophys. Res. **124**(11), 11232–11250, https://doi.org/10.1029/2019JB018238 (2019).
[36]D. B. Ghosh and B. B. Karki, "Effects of valence and spin of Fe in $MgSiO_3$ melts: Structural insights from first-principles molecular dynamics simulations," Geochim. Cosmochim. Acta **279**, 107–118 (2020).
[37]G.-H. Zhang, K.-C. Chou, and K. Mills, "Modelling viscosities of CaO–MgO–Al_2O_3–SiO_2 molten slags," ISIJ Int. **52**(3), 355–362 (2012).
[38]C. J. B. Fincham, F. D. Richardson, and C. F. Goodeve, "The behaviour of sulphur in silicate and aluminate melts," Proc. R. Soc. London Ser. A **223**(1152), 40–62 (1997).
[39]J. López-Rodríguez, A. Romero-Serrano, A. Hernández-Ramírez, M. Pérez-Labra, A. Cruz-Ramírez, and E. Rivera-Salinas, "Use of a structural model to calculate the viscosity of liquid silicate systems," ISIJ Int. **58**(2), 220–226 (2018).
[40]S. Le-Roux, see https://atomes.ipcms.fr/ for "Atomes" (2024).
[41]M. Sajid, C. Bai, M. Aamir, Z. You, Z. Yan, and X. Lv, "Understanding the structure and structural effects on the properties of blast furnace slag (BFS)," ISIJ Int. **59**(7), 1153–1166 (2019).
[42]C. J. Benmore, R. Bogle, S. K. Wilke, R. Weber, J. Neuefeind, and G. Costa, "The structure of CaO–MgO–Al_2O_3–SiO_2 melts and glasses doped with FeO–NiO," J. Am. Ceram. Soc. **107**(9), 6323–6333 (2024).
[43]G. Demazeau, A. Baranov, I. Presniakov, and A. Sobolev, "High oxygen pressures and the stabilization of the highest oxidation states of transition metals—Mössbauer spectroscopic characterization of the induced electronic phenomena," Z. Nat. B **61**(12), 1527–1540 (2006).
[44]M. Okube, Y. Furukawa, A. Yoshiasa, T. Hashimoto, M. Sugahara, and A. Nakatsuka, "Oxidation state and effective pair potential of Fe^{4+} ions in perovskite-type $SrFeO_3$ annealed under high oxygen pressure," J. Phys.: Conf. Ser. **121**(9), 092004 (2008).
[45]S. E. Boland, S. K. Wilke, J. A. Scott, S. M. Schlossberg, A. Ivaschenko, R. J. K. Weber, and D. W. Lipke, "A hyperbaric aerodynamic levitator for containerless materials research," Rev. Sci. Instrum. **94**(5), 053903 (2023).
[46]W. A. Phelan, J. Zahn, Z. Kennedy, and T. M. McQueen, "Pushing boundaries: High pressure, supercritical optical floating zone materials discovery," J. Solid State Chem. **270**, 705–709 (2019).